

Effects of Crystal Phase Mixing on the Electrical Properties of InAs Nanowires

Claes Thelander,^{*,†} Philippe Caroff,[‡] Sébastien Plissard,^{‡,§} Anil W. Dey,^{||} and Kimberly A. Dick^{†,⊥}

[†]Solid State Physics, Lund University, Box 118, S-221 00 Lund, Sweden

[‡]Institut d'Electronique, de Microélectronique et de Nanotechnologie, UMR CNRS 8520, Avenue Poincaré, B.P. 60069, 59652 Villeneuve d'Ascq, France

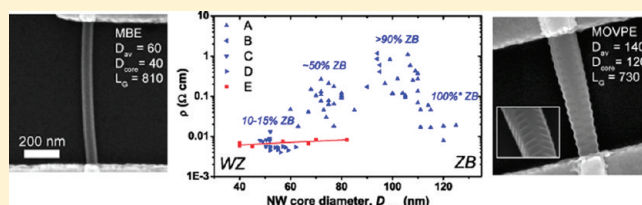
[§]Department of Applied Physics, Photonics and Semiconductor Nanophysics, Eindhoven University of Technology, P.O. Box 513, NL-5600 MB Eindhoven, Netherlands

^{||}Department of Electrical- and Information Technology, Lund University, Box 118, 221 00, Lund, Sweden

[⊥]Polymer & Materials Chemistry, Lund University, Box 124, S-221 00 Lund, Sweden

ABSTRACT: We report a systematic study of the relationship between crystal quality and electrical properties of InAs nanowires grown by MOVPE and MBE, with crystal structure varying from wurtzite to zinc blende. We find that mixtures of these phases can exhibit up to 2 orders of magnitude higher resistivity than single-phase nanowires, with a temperature-activated transport mechanism. However, it is also found that defects in the form of stacking faults and twin planes do not significantly affect the resistivity. These findings are important for nanowire-based devices, where uncontrolled formation of particular polytype mixtures may lead to unacceptable device variability.

KEYWORDS: Nanowire, InAs, crystal structure, zinc blende, wurtzite, transport



Binary semiconductor nanowires are known to exhibit high densities of randomly arranged stacking defects when grown epitaxially in a close-packed direction. For the case of III–V materials, nanowires are most often composed of mixtures of cubic zinc blende (ZB) and hexagonal wurtzite (WZ) crystal phases, together with high densities of twin planes and stacking faults. Theoretical predictions have indicated that ZB and WZ phases have different electronic band structures,^{1–4} and that stacking defects and phase boundaries should act as scattering centers for electrons during 1D transport.⁵ Indeed, optical investigations of InP^{6,7} and GaAs^{8–10} nanowires have clearly indicated differences in optical emission for the different crystal phases. In accordance with this, extensive efforts have been directed toward control and tuning of crystal phase in all III–V nanowire materials for all growth systems.¹¹ However, to date, the impact of structural variation on electron transport has not been clarified for III–V materials.

Nanowires of InAs are of particular interest for electronic applications due to favorable bulk properties, such as high mobility and injection velocities, and for the low contact resistance.^{12,13} With the polytypism typically observed in nanowires, it is crucial to understand the effects of crystal phase and random structural variations on charge transport in this material. Modeling of the electronic band structure of InAs indicates that the band gap of WZ is larger than that of ZB,^{1–3} with an approximately 30–90 meV discontinuity in the conduction band.^{1,3} There have been a few recent experimental studies which have attempted to correlate variation in electrical properties with crystal structure in InAs.^{14–16}

In these cases it was found that nanowires with a mixed crystal structure indeed had properties that indicated the presence of barriers for the electron transport. So far however, studies have focused on only a limited selection of nanowire crystal structures. As well, the attainment of different phases for comparison has required changes in growth parameters, and even growth direction, which in turn led to variations in background carbon dopant incorporation from the metalorganic precursors used in these studies.¹⁷ Therefore, it has not yet been possible to unambiguously determine the effect of crystal phase and stacking defects on electron transport in InAs nanowires.

In this study we investigate electron transport in InAs nanowires grown by metalorganic vapor phase epitaxy (MOVPE) with crystal structure ranging from WZ with low stacking fault density to ZB with a periodic twinning structure. This structure variation is attained by growing nanowires using Au seed particles of different diameters, in order to tune the structure from WZ to ZB without changing growth conditions. To account for any diameter effects not related to structure, we also consider nanowires with close to pure WZ phase grown by molecular beam epitaxy (MBE), which only exhibit very subtle diameter effects on structure and do not suffer from carbon background doping.

Received: March 12, 2011

Revised: April 21, 2011

We observe that the addition of a small amount of WZ phase (1%) to ZB nanowires is profound, causing an increase in electrical resistivity of 2 orders of magnitude (up to $1 \Omega \text{ cm}$). Further increase of the WZ phase leads to a decrease in resistivity, but with a magnitude still far above that of the pure ZB phase and with a considerable scatter in the data. By contrast, we find that WZ nanowires containing up to 15% ZB phase, primarily in the form of stacking faults, have resistivity very similar to the MBE-grown nanowires and also show a very small spread in resistivity. Temperature-dependent measurements for nanowires in the transition region to ZB, with a very small fraction of WZ in the form of extended segments, indicate an activation energy of 45 meV, which agrees well with results from modeling using a Poisson solver.

Furthermore, it is found that ZB nanowires free from WZ, but with a periodic twinning superlattice, have resistivity values on the same order as pure WZ nanowires, which shows that twins have a much smaller effect on the transport than mixtures of extended WZ/ZB segments. The results presented here clearly demonstrate that a randomly mixed structure would be detrimental to advanced devices; however controlled mixtures, such as designed barriers and quantum wells, may have interesting applications.¹⁸

Table 1. Growth Parameters, Nanowire Dimensions, and Total Number of Devices Included in the Study

growth	TMIn (10^{-6} m.f.)	V/III	D_{av} (nm)	D_{core} (nm)	devices
A, MOVPE	3.0	130	60–150	60–125	48
B, MOVPE	6.9	40	95–105	90–95	5
C, MOVPE	3.0	90	48–52	48–52	9
D, MOVPE	3.0	50	52–65	52–62	10
E, MBE		(2)	50–82	40–82	8

Five types of nanowire samples were investigated as listed in Table 1. Samples A–D were grown in a standard commercial metal organic vapor phase epitaxy (MOVPE) reactor at 10 kPa using gold particles as seed material. First, size-selected gold aerosol particles were deposited onto InAs (111)B substrates at an approximate surface density of one particle per square micrometer; in the case of sample A, a range of gold particle sizes was used. After gold deposition, the substrates were transferred to the MOVPE reactor. All samples were grown at 480 °C on InAs-(111)B substrates, without special annealing steps. Trimethylindium (TMIn) and arsine (AsH_3) were used as precursor molecules, with growth conditions as listed in Table 1; V/III ratios listed for MOVPE samples are based on the precursor fluxes.

Sample E was grown by gas source MBE on top of a short InP nanowire stem on InP(111)B substrates. A thin gold film (3 Å) was evaporated ex situ by electron beam onto the substrates prior to introduction into the reactor. Gold droplets self-formed during the annealing and deoxidation step at 525 °C under P_2 flux, by dewetting of the gold film. V/III ratios were calculated from 2D equivalent growth rates, calibrated by reflection high energy electron diffraction (RHEED) and set to 2.0–2.2 for InP and InAs, using an indium flux corresponding to 0.5 ML/s 2D equivalent growth rate. InP stem growth was initiated at 410 °C, and InAs nanowires were subsequently grown by direct switch from P_2 to As_2 molecular fluxes. Growth times of 15 and 80 min for InP and InAs, respectively, result in 80–130 nm InP stem (diameter dependent length) and $4.50 \pm 0.2 \mu\text{m}$ long InAs segments, where the InP stem is fully buried under 2D overgrowth on the substrate.

High-resolution transmission electron microscopy (HRTEM) was used to investigate all of the samples in this study. The HRTEM images were acquired with a 300 kV field emission gun TEM (JEM 3000F) with a point resolution of 1.6 Å. The images were recorded along the $\langle 110 \rangle$ zone axis in the cubic cell using a $2\text{k} \times 2\text{k}$ CCD camera. Samples for HRTEM were obtained by

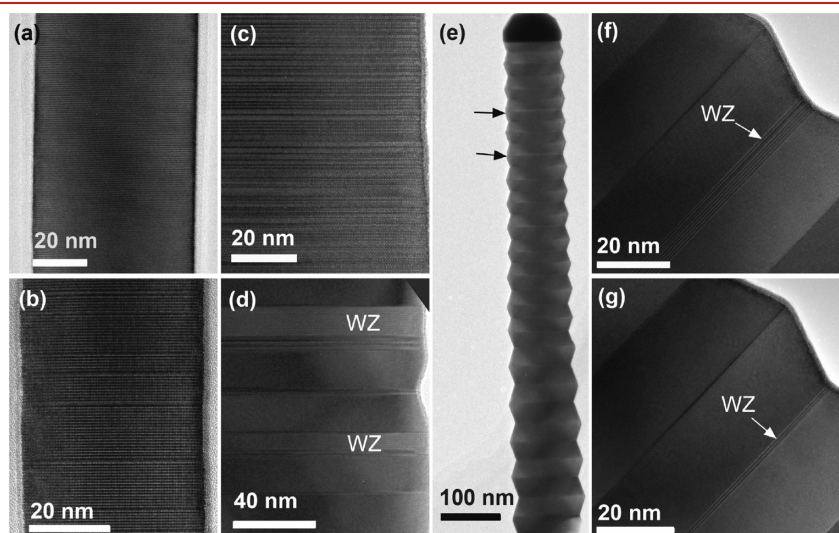


Figure 1. TEM images illustrating the effect of growth technique and diameter on InAs nanowire crystal structure. All diameters measurements refer to the core diameter measured at the particle–nanowire interface: (a) 56 nm nanowire grown by MBE, exhibiting WZ structure with on average 2 stacking faults per micrometer; (b) 46 nm diameter nanowire grown by MOVPE, exhibiting WZ crystal structure with 115 stacking faults per micrometer; (c) 73 nm diameter MOVPE nanowire, exhibiting mixed WZ and ZB crystal phase; (d) 96 nm diameter MOVPE nanowire, exhibiting predominantly ZB phase but with WZ segments up to 15 nm long representing 5% of the nanowire structure; (e) 112 nm diameter MOVPE nanowire, exhibiting predominantly ZB structure with periodic twin planes and two individual WZ segments indicated by arrows, twin planes and WZ segments in total represent about 1% of the nanowire structure; (f) high-magnification image of the WZ segment indicated by the uppermost arrow in (e), this segment is about 6 nm long; (g) high-magnification image of the WZ segment indicated by the lower arrow in (e), this segment is about 2 nm long.

depositing nanowires onto carbon film coated Cu grids, by gently rubbing the grid against the sample, in most cases breaking the nanowires off at the base.

Particle-seeded nanowires are understood to grow layer-by-layer, so variations in the stacking sequence occur when sequential nuclei at the particle–wire interface are rotated into different orientations.¹⁹ It has been determined that this structural variation is diameter-dependent, with WZ phase occurring predominantly at smaller diameters and ZB at larger.²⁰ All nanowires in this study exhibit radial overgrowth to a varying degree, meaning that the average diameter, D_{av} , of the nanowire is larger than the diameter at the particle–wire interface. However, since it is the diameter of the particle–nanowire interface that determines the crystal structure,²¹ it is this core diameter, D_{core} , that is intended when we refer to diameter below, unless otherwise noted.

TEM investigations showed that the MOVPE-grown nanowires in this study have a predominantly WZ structure at the smallest diameters studied, with stacking faults which increase in density with diameter (Figure 1b). As D_{core} is increased above 50 nm, thicker and more frequent ZB segments appear, and by 70 nm the nanowires exhibit random mixtures of WZ and ZB segments, with an overall average of about 50% WZ phase and considerable structural variation between and within individual nanowires (Figure 1c). By 80 nm diameter, ZB makes up about 85% of the nanowire phase, but twin planes are very frequent with average ZB segment length of only a few nanometers, and WZ segments appearing regularly. By 90 nm, ZB segments typically exhibit a constant maximum length (around 15 nm) with periodically arranged twin planes. WZ segments of about 10 nm average length still appear rather frequently at random positions (Figure 1d). Nanowires larger than 100 nm diameter exhibit a periodically twinned structure, with ZB segments of a constant length (around 20 nm, increasing slightly with diameter) separated by twin planes (Figure 1e). However, WZ segments are still observed at the interface between ZB twin segments. For 110 nm diameter these segments have a typical length of 5 nm and occur on average about twice per micrometer of length, so they constitute about 1% of the nanowire crystal phase (Figures 1f,g). For diameters above 120 nm, no WZ segments are observed along the entire length, and the nanowires have perfect periodically twinned ZB structure with alternating $\{111\}A$ and $\{111\}B$ facets.

We have previously observed that parameters such as temperature and V/III ratio affect resistivity in a way that may be attributed to changes in background carbon, independent of crystal structure.¹⁷ The bulk of the data was therefore obtained from a single growth; however, other growths, with different V/III ratios, were used to improve the statistics for certain key diameter regions (D_{core} : 50–60 nm and 90–95 nm) and to verify observed trends.

Nanowires grown by MBE were also considered in this study in order to clearly separate changes in crystal structure from changes in background doping and diameter. MBE-grown InAs nanowires exhibit high-quality WZ phase for all diameters (Figure 1a), similar to that observed for nanowires grown by chemical beam epitaxy (CBE).¹⁷ Only a very subtle change in crystal structure with diameter is observed, from zero stacking faults (pure WZ phase) at D_{core} below about 40 nm, to about 15 stacking faults per micrometer length for diameter around 80 nm. This is still an order of magnitude fewer stacking faults than in all of the nanowires grown by MOVPE for this study.

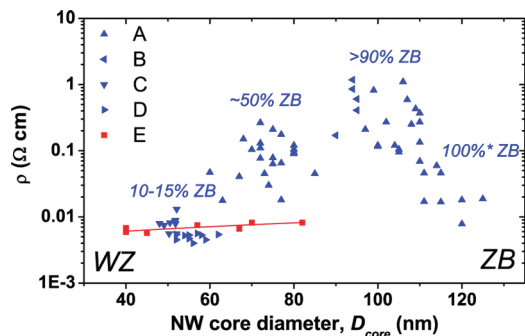


Figure 2. Nanowire resistivity, ρ , plotted against nanowire core diameter, D_{core} , for five different sets of nanowires. With increasing diameter the structural composition of the MOVPE nanowires (types A–D) undergoes a transition from WZ, with 100–150 stacking faults per micrometer, to a pure, but periodically twinned, ZB structure. A peak in the resistivity is observed for $D_{core} \sim 100$ nm. The MBE wires (type E) have pure WZ crystal structure for the smallest diameters, and about 15 stacking faults per micrometer for the largest (80 nm) nanowires. The red line is a linear fit to the MBE data.

For electrical characterization nanowires were transferred to degenerately n-doped (P) Si samples with a 100 nm SiO_2 insulating surface layer. Suitable nanowires were identified by low-resolution scanning electron microscopy (SEM) inspection and selected for contact processing. The samples were spin-coated with an electron-beam sensitive polymer, and contacts were exposed to the selected nanowires using electron beam lithography. The InAs nanowire contact areas were etched for 2 min in a mixture of $(\text{NH}_4)_2\text{S}_x$ and H_2O 1:9 heated to 40 °C, and rinsed in water. A film of 25 nm Ni and up to 150 nm Au was evaporated onto the samples followed by lift-off in acetone. The samples were finally glued to chip carriers and wire bonded for electrical measurements. SEM inspection was also carried out after the electrical characterization, where the nanowire diameter, D_{av} , was obtained by averaging the diameter of a nanowire over its free length, L_G , between the contacts. Values for the nanowire resistivity were obtained by approximating the nanowires with a cylindrical geometry, $\rho = R\pi D_{av}^2/4L_G$, where R is the nanowire resistance measured at a drain voltage, $V_D = 10$ mV, and a back-gate voltage, $V_G = 0$ V. The nanowire core diameter, D_{core} , was obtained by measuring the nanowire diameter below the gold particle where no overgrowth was present. Electrical measurements were carried out with the samples located in an evacuated chamber under darkness.

The data for resistivity was here analyzed in terms of D_{core} , as this parameter primarily determines the crystal structure of Au-nucleated InAs nanowires for given growth conditions. Electrical measurements of nanowires of type E (MBE), with close to 100% WZ, gave uniform resistivity values in the whole range of studied core diameters as seen in Figure 2, between 6 and 8×10^{-3} Ω cm. The nanowires of types C and D (MOVPE) in Figure 2 were characterized as a part of a larger study,¹⁷ where InAs nanowires grown under various conditions in MOVPE and CBE were investigated. In that study it was found that nanowires, in a limited diameter range from 40 to 60 nm, with a WZ fraction that varies from 100 to 85%, typically have a measured resistivity between 4 and 10×10^{-3} Ω cm. For such nanowires, the ZB primarily occurs only in very short segments, typically as stacking faults. These nanowires show rather similar resistivity values to

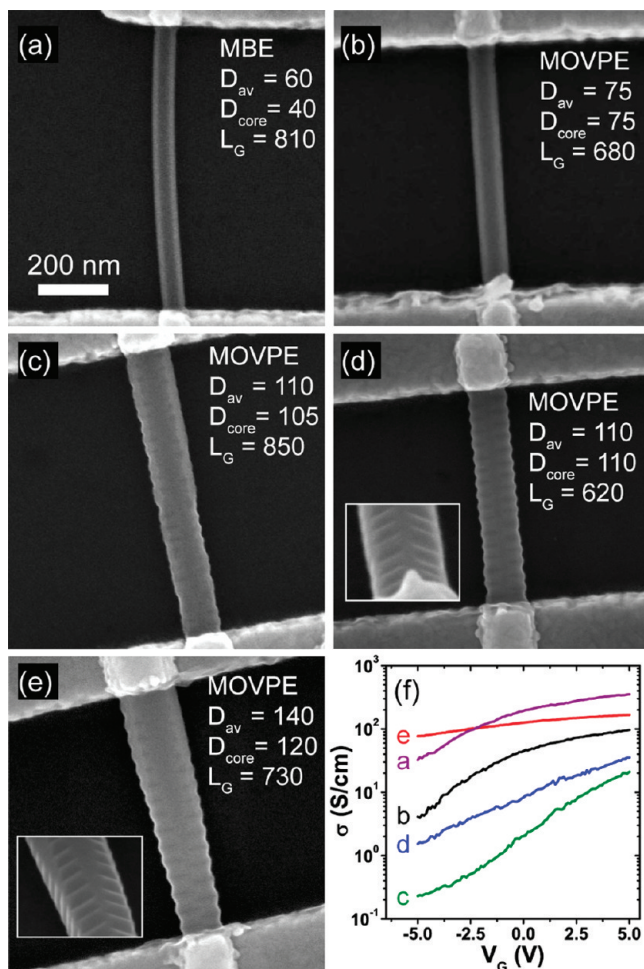


Figure 3. Top-view SEM images of InAs nanowires contacted by pairs of electrodes, with similar magnification. (a) MBE nanowire of type E. (b–e) MOVPE nanowires of type A. The nanowires in panels c–e show a twinning superlattice, with a lattice periodicity in panels c and d that is less perfect than that in panel e. The two insets in panels d and e were recorded with a tilt of 52° . (f) Conductivity, $\sigma = 1/\rho$, as a function of V_G , measured at $V_D = 10$ mV and $T = 295$ K, for the nanowires in (a–e).

the MBE-grown nanowires, which indicates that the presence of stacking faults and short ZB segments in predominantly WZ nanowires does not dramatically affect the electrical properties, although here to some degree likely compensated by carbon doping.

Nanowires of types A and B (MOVPE), with higher fractions of ZB, behave very differently from the other nanowires studied. As D_{core} increases from 60 to 100 nm the resistivity shows a strong increase, and notably also a very large spread. Despite a considerable increase in nanowire diameter, and thus cross-sectional area available for conduction, the overall device resistivity also typically increased. However, for nanowires with $D_{\text{core}} > 110$ nm a sharp decline in the resistivity is observed, and some data points for the very largest studied diameters almost reach the same resistivity values as in the case of pure WZ nanowires. For these diameters TEM inspection indicates a ZB phase with periodic twins, free from WZ inclusions.

Some of the spread in resistivity observed between the different sets of MOVPE-grown nanowires may be attributed to a change in V/III ratio. However, sets A and B, with dissimilar V/III ratios, both

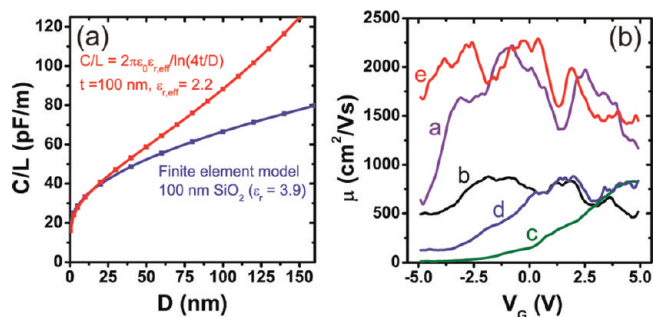


Figure 4. (a) Back-gate capacitance as a function of diameter for metallic nanowires on a 100 nm SiO_2 dielectric, extracted using an analytical (red) and a finite element model (blue), respectively. (b) Field-effect mobility as a function of back-gate voltage extracted for the nanowires in panels a–e of Figure 3.

show very high resistivity values for similar D_{core} (95–105 nm), whereas sets B and D, with similar V/III but dissimilar D_{core} (B, 55 nm; D, 95 nm) have a 2 orders of magnitude difference in resistivity. This shows that the effect of V/III ratio is much smaller than effects of structure for the case of mixed-structure nanowires.

Another potential uncertainty in the study was that large diameter nanowires may disrupt electrodes fabricated by the lift-off technique and give unreliable contacts. However, the fact that the resistivity dropped considerably for the very thickest nanowires indicates that this was not the case, which was also verified by measurements on nanowires with multiple contacts. Furthermore, the lowest observed resistivity values were most often linked to the shortest nanowire segments, which is contrary to what one would expect if contact resistance dominated. This indicates that the high resistivity was an intrinsic property of the nanowires, likely a result of the mixed crystal structure; the shorter the length of integration the more evident is the existence of a statistical spread in the relative mixing of the two crystal structures. This also explains the very large spread in the resistivity data observed for nanowires in the intermediate diameter range where structural characterization in TEM showed a substantial wire-to-wire, and intrawire variation in the mixing of crystal phases.

Figure 3f shows the nanowire conductivity ($1/\rho$) as a function of back-gate voltage for four different nanowires grown by MOVPE, and one wire grown by MBE. The examples were selected to highlight the differences in observed electrical properties as the diameter and crystal structure are changed. The nanowires in panels c and d of Figure 3, with core diameters of 105 and 110 nm, seem to be in the subthreshold regime for most gate voltages, whereas nanowires that are thinner (Figure 3a,b) and thicker (Figure 3e), instead show signs of on-current saturation. This indicates that one or several barriers block the transport even for positive V_G for the nanowires in Figure 3c,d.

Values for nanowire back-gate capacitance and mobility were extracted for the nanowires in Figure 3. In Figure 4a we compare the results of a commonly used analytical model, with results from a finite element model (Comsol Multiphysics) for extraction of nanowire capacitance per unit length. The analytical model, $C/L = 2\pi\epsilon_0\epsilon_r,\text{eff}/\ln(4t/D)$, is accurate ($<1\%$ error) for nanowire diameters, $D < t/3$ ($t = 100$ nm SiO_2), provided an effective relative dielectric constant $\epsilon_r,\text{eff} = 2.2$ is used to compensate that the nanowire is not fully embedded in SiO_2 ($\epsilon_r = 3.9$).²² Because of the large error for thick nanowires, capacitance

values from the finite element model were used to extract the field-effect mobility, μ , of the nanowires in Figure 3, using $\mu = (dI/dV_G)L_G^2/(CV_D)$. Figure 4b shows that the extracted mobility values for the nanowires in panels a (WZ) and e (ZB) of Figure 3 are roughly 3 times larger than those for the mixed-phase nanowires in panels b–d of Figure 3 within the measured gate voltage span. This supports the interpretation that a mixed crystal structure is resulting in significant carrier scattering.

We note that for some ZB nanowires, the alternating $\{111\}$ A and $\{111\}$ B facets (Figure 1e–g) have overgrown to eventually have flat $\{110\}$ facets, such as the upper regions of the nanowires in Figure 3c,e (base of the nanowires; see also Figure 3e inset). Such overgrowth typically starts to develop at the base of a nanowire and then propagates along its length as the nanowire grows. However, no systematic effects on the electrical properties have been observed as a result of such overgrowth, even in cases where the nanowires have fully developed $\{110\}$ facets.

An intriguing explanation to the sudden decrease in resistivity for the very largest diameters, where TEM shows formation of a clean, periodic twin-plane superlattice, is that such wires could be expected to show minibands of allowed electron states.²³ However, the transport in these cases showed behavior very similar to WZ nanowires with regards to changes in temperature ($4.2 < T < 295$ K), biasing conditions ($0 < V_D < 0.5$ V), and back-gate sweeps, which we believe is unlikely for miniband transport. The more likely explanation is that the decrease in resistivity is due to a lack of WZ inclusions that would act as barriers for electron transport. To verify such an effect, nanowires in the transition region were further investigated by temperature-dependent transport measurements. The results presented here are for the nanowire shown in Figure 3d with $D_{\text{core}} = 110$ nm, and for which some interruptions are visible in the otherwise periodic faceting, likely due to WZ inclusions. Back-gate sweeps were recorded for $V_D = 10$ mV, in the range $120 \text{ K} < T < 250$ K, as shown in Figure 5a. The T dependence of the I – V_G curves indicates a temperature activated mechanism such that $I = I_0 e^{-E_a/kT}$, where E_a is the activation energy and $k = 8.62 \times 10^{-5}$ eV/K.

Figure 5c shows E_a as a function of V_G , where E_a was extracted from linear fits to the data in Figure 5b. A decrease in E_a from around 100 meV down to 10 meV is deduced for the studied V_G range, which we interpret as a decrease in the effective barrier height in the conduction band relative to E_F . For $V_G = 0$ the activation energy is around 40–50 meV relative to the Fermi level. We find this number to be reasonable based on the theoretical predictions for the ZB–WZ conduction band offset.^{1,3}

How can we explain that, separately, both pure WZ and ZB nanowires have transport properties as though they were degenerately doped, whereas mixtures of WZ and ZB show much higher resistivity values? One possible mechanism is polarization charges at the WZ/ZB interfaces, as discussed by Dayeh et al.,¹⁴ that would create a sawtooth potential in the conduction and valence bands along the length of a nanowire. This mechanism was proposed to explain the much weaker pinch-off properties observed for ZB nanowires grown at 350 °C, as compared to polytypic WZ/ZB InAs nanowires grown at 500 °C. In previous work we reported that growth of InAs nanowires at 380 °C leads to a clean ZB crystal structure, and where a method of controlled In supply interrupts can be used to induce growth of WZ segments.¹⁶ However we also found that nanowires grown at such low temperatures with TMI_n as In precursor had a substantial carbon (n) doping. In that case E_F with respect to the InAs conduction band edge had to be considerably lowered by use of a

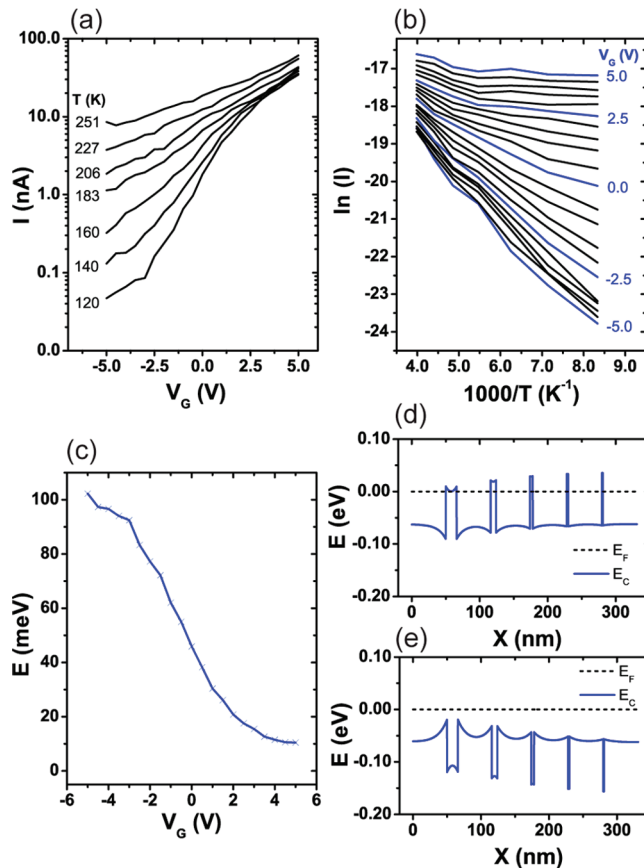


Figure 5. (a) I – V_G sweeps recorded for temperatures between 120 and 251 K for the nanowire in Figure 3d with a twin plane superlattice, but with some visible interrupts. (b) The data in panel a plotted as $\ln(I)$ against $1000/T$. (c) Activation energy obtained from linear fits to the data in panel b, plotted as a function of V_G . (d) Results of Poisson calculations for the conduction band energy for WZ segments with decreasing lengths of 16, 8, 4, 2, 1 nm in ZB. (e) Corresponding result for the opposite case of ZB segments (16, 8, 4, 2, 1 nm) in WZ.

back-gate to observe effects of the WZ segments on the transport. The pinch-off voltages for such nanowires with designed tunnel barriers of WZ in ZB were almost identical ($-25 \text{ V} < V_G < -20 \text{ V}$) to that of pure reference ZB nanowires. This indicates that possible effects of polarization charges at the surface of such thin (4 nm) WZ segments were not strong enough to compensate for the carbon doping and have a measurable effect on the band structure.

Another possible contribution to the observed effect of WZ/ZB polytypism could be based on the presence of donor states situated far up in the conduction band for InAs,²⁴ well above both the ZB and WZ conduction band minimum. A Poisson solver²⁵ was used to model the band structure of ZB and WZ segments of various lengths, based on two sets of assumptions: First, that the density of such surface states is approximately the same for both WZ and ZB, here set to result in a nanowire carrier concentration of $n_{\text{WZ}} = n_{\text{ZB}} = 3 \times 10^{17} \text{ cm}^{-3}$, which corresponds to a surface donor state density of $8 \times 10^{11} \text{ cm}^{-2}$ for a $D = 100$ nm nanowire. Second, we assume a staggered band line-up between WZ and ZB with a conduction band offset of 100 meV, with band gap energies $E_g(\text{WZ}) = 0.42$ eV and $E_g(\text{ZB}) = 0.37$ eV. Figure 5d shows the resulting conduction band profile for a ZB nanowire with WZ segments of decreasing thicknesses: 16, 8, 4, 2, and

1 nm. Conversely, Figure 5e represents the results for a WZ nanowire with ZB segments of corresponding lengths.

The first case, Figure 5d, gives barriers for the carriers, with a height that varies from 40 meV (1 nm) to 10 meV (16 nm) with respect to E_F . The varying barrier height is a result of band bending at the interfaces of the two types of segments as electrons accumulate in the ZB close to the WZ in the model. Further simulations showed that this effect would be present, although weaker, for n_{ZB} up to $1 \times 10^{18} \text{ cm}^{-3}$ ($n_{WZ} = 3 \times 10^{17} \text{ cm}^{-3}$), at which point E_F is above the conduction band edge of all WZ segments. Again, we interpret that such a situation was observed as a result of strong carbon doping for the nanowires grown at 380 °C, where designed WZ segments did not act as tunnel barriers unless V_G was made very negative.¹⁶

Modeling of the second case, Figure 5e, shows that long ZB segments in predominantly WZ nanowires also can have a strong effect on the band structure near E_F and result in considerable scattering. On the other hand, short ZB segments do not seem to lead to the same local decrease in $E_F - E_C$. The model has assumed a uniform radial carrier concentration in the nanowires. In reality, there is likely a radial band bending in addition to the axial, in which case the barrier height is lower at the surface and higher in the center of the wire.

In summary, InAs nanowires were grown by MOVPE from a range of gold particle diameters, resulting in nanowires with a diameter-dependent range of WZ/ZB fractions as observed by TEM. On the basis of transport measurements of such nanowires and of reference WZ nanowires grown by MBE, it was found that crystal defects in the form of stacking faults in WZ and twin planes in ZB do not seem to have a significant effect on the room-temperature resistivity of InAs nanowires. However, extended WZ segments in predominantly ZB nanowires were observed to have a very strong effect on transport, increasing the resistivity by up to 2 orders of magnitude. On the basis of temperature-dependent measurements the WZ conduction band edge relative to E_F was estimated at around 45 meV for the nanowires grown at 480 °C. This is in contrast to previously reported results on InAs nanowires grown at 380 °C where no barrier could be found at $V_G = 0$ due to a high doping background.¹⁶

The study clearly shows that the nature of a crystal defect and surrounding carrier concentration determine how, and to which extent, the transport is affected. This is important for development and studies of nanowire devices, such as field-effect transistors (FETs), where uncontrolled polytypism in the gated segment will likely lead to considerable device variability, whereas effects of corresponding polytypism in the heavily doped source and drain segments will be negligible. On the other hand, controlled design of the crystal phase along the length of a wire could be used to tailor the device properties, such as providing a low barrier segment for carriers to suppress off-currents.²⁶

AUTHOR INFORMATION

Corresponding Author

*Electronic mail: claes.thelander@ftf.lth.se.

ACKNOWLEDGMENT

This work received financial support from the Nanometer Structure Consortium at Lund University (nmC@LU), the Swedish Research Council (VR), the Swedish Foundation for Strategic Research (SSF), and the Knut and Alice Wallenberg

Foundation (KAW). The authors would like to thank Mats-Erik Pistol, Jessica Bolinsson, Lars Samuelson, and Jesper Wallentin for valuable discussions.

REFERENCES

- (1) Murayama, M.; Nakayama, T. *Phys. Rev. B* **1994**, *49*, 4710–4724.
- (2) Zanolli, Z.; Fuchs, F.; Furthmüller, J.; von Barth, U.; Bechstedt, F. *Phys. Rev. B* **2007**, *75*, 245121.
- (3) De, A.; Pryor, C. E. *Phys. Rev. B* **2010**, *81*, 155210.
- (4) Akiyama, T.; Yamashita, T.; Nakamura, K.; Ito, T. *Nano Lett.* **2010**, *10*, 4614–4618.
- (5) Stiles, M. D.; Hamann, D. R. *Phys. Rev. B* **1990**, *41*, 5280–5282.
- (6) Mishra, A.; V. Titova, L.; Hoang, T. B.; Jackson, H. E.; Smith, L. M.; Yarrison-Rice, J. M.; Kim, Y.; Joyce, H. J.; Gao, Q.; Tan, H. H.; Jagadish, C. *Appl. Phys. Lett.* **2007**, *91*, 263104.
- (7) Bao, J. M.; Bell, D. C.; Capasso, F.; Wagner, J. B.; Martensson, T.; Tragardh, J.; Samuelson, L. *Nano Lett.* **2008**, *8*, 836.
- (8) Hoang, T. B.; Moses, A. F.; Zhou, H. L.; Dheeraj, D. L.; Fimland, B. O.; Weman, H. *Appl. Phys. Lett.* **2009**, *94*, 133105.
- (9) Heiss, M.; *Phys. Rev. B* **2011**, *83*, 045303.
- (10) Parkinson, P.; Joyce, H. J.; Gao, Q.; Tan, H. H.; Zhang, X.; Zou, J.; Jagadish, C.; Herz, L. M.; Johnston, M. B. *Nano Lett.* **2009**, *9*, 3349.
- (11) Caroff, P.; Bolinsson, J.; Johansson, J. *IEEE J. Sel. Top. Quantum Electron.* DOI: 10.1109/JSTQE.2010.2070790.
- (12) Thelander, C.; Björk, M. T.; Larsson, M. W.; Hansen, A. E.; Wallenberg, L. R.; Samuelson, L. *Solid State Commun.* **2004**, *131*, 573–579.
- (13) Thelander, C.; Fröberg, L. E.; Rehnstedt, C.; Samuelson, L.; Wernersson, L. E. *IEEE Electron Device Lett.* **2008**, *29*, 206–208.
- (14) Dayeh, S. A.; Susac, D.; Kavanagh, K. L.; Yu, E. T.; Wang, D. *Adv. Funct. Mater.* **2009**, *19*, 2102–2108.
- (15) Schroer, M. D.; Petta, J. R. *Nano Lett.* **2010**, *10*, 1618–1622.
- (16) Dick, K. A.; Thelander, C.; Samuelson, L.; Caroff, P. *Nano Lett.* **2010**, *10*, 3494–3499.
- (17) Thelander, C.; Dick, K. A.; Borgström, M. T.; Fröberg, L. E.; Caroff, P.; Nilsson, H. A.; Samuelson, L. *Nanotechnology* **2010**, *21*, 205703.
- (18) Lin, Y. M.; Dresselhaus, M. S. *Phys. Rev. B* **2003**, *68*, 075304.
- (19) Glas, F.; Harmand, J. C.; Patriarche, G. *Phys. Rev. Lett.* **2007**, *99*, 146101.
- (20) Johansson, J.; Dick, K. A.; Caroff, P.; Messing, M. E.; Bolinsson, J.; Deppert, K.; Samuelson, L. *J. Phys. Chem. C* **2010**, *114*, 3837–3842.
- (21) Shtrikman, H.; Popovitz-Biro, R.; Kretinin, A.; Heiblum, M. *Nano Lett.* **2009**, *9*, 1506.
- (22) Wunnicke, O. *Appl. Phys. Lett.* **2006**, *89*, 083102.
- (23) Ikonc, Z.; Srivastava, G. P.; Inkson, J. P. *Phys. Rev. B* **1993**, *48*, 17181–17193.
- (24) Weber, J. R.; Janotti, A.; Van de Walle, C. G. *Appl. Phys. Lett.* **2010**, *97*, 192106.
- (25) Tan, I. –H.; Snider, G. L.; Hu, E. L. *J. Appl. Phys.* **1990**, *68*, 4071–4076.
- (26) Lind, E.; Persson, A. I.; Samuelson, L.; Wernersson, L.-E. *Nano Lett.* **2006**, *6*, 1842–1846.